

Cite this: *Energy Environ. Sci.*, 2011, **4**, 4270

www.rsc.org/ees

PAPER

Photocatalytic water oxidation with suspended alpha-Fe₂O₃ particles-effects of nanoscaling

Troy K. Townsend,^a Erwin M. Sabio,^a Nigel D. Browning^{bc} and Frank E. Osterloh^{*a}

Received 10th July 2011, Accepted 28th July 2011

DOI: 10.1039/c1ee02110a

Alpha-Fe₂O₃ is cheap and abundant, and has a visible light indirect (phonon assisted) band gap of 2.06 eV (600 nm) due to a d-d transition, and a direct band gap at 3.3 eV (375 nm), associated with the ligand to metal charge transfer process. Here we describe results on using freely dispersed Fe₂O₃ nanocrystals for photocatalytic water oxidation. Three morphologies of hematite were compared, including bulk-type- α -Fe₂O₃ (Bulk-Fe₂O₃, 120 nm), ultrasonicated Bulk-Fe₂O₃ (Sonic-Fe₂O₃, 44 nm), and synthetic Fe₂O₃ (Nano-Fe₂O₃, 5.4 nm) obtained by hydrolysis of FeCl₃·6H₂O. According to X-ray diffraction, all phases were presented in the alpha structure type, with Nano-Fe₂O₃ also containing traces of β -FeOOH. UV/Vis diffuse reflectance revealed an absorption edge near 600 nm ($E_G = 2.06$ eV) for all materials. Cyclic voltammetry gave the water oxidation overpotentials (*versus* NHE at pH = 7, at 1.0 mA cm⁻²) as $\eta = +0.43$ V for Nano-Fe₂O₃, $\eta = +0.63$ V for Sonic-Fe₂O₃, and $\eta = +0.72$ V for Bulk-Fe₂O₃. Under UV and visible irradiation from a 300 W Xe-arc lamp, all three materials (5.6 mg) evolved O₂ from water with 20.0 mM aqueous AgNO₃ as sacrificial electron acceptor. The highest rates were obtained under UV/Vis (>250 nm) irradiation with 250 $\mu\text{mol h}^{-1} \text{g}^{-1}$ for Bulk-Fe₂O₃, 381 $\mu\text{mol h}^{-1} \text{g}^{-1}$ for Sonic-Fe₂O₃ and 1072 $\mu\text{mol h}^{-1} \text{g}^{-1}$ for Nano-Fe₂O₃. Turnover numbers (TON = moles O₂/moles Fe₂O₃) were above unity for Nano-Fe₂O₃ (1.13) and Sonic-Fe₂O₃ (1.10) but not for Bulk-Fe₂O₃ (0.49), showing that the nanoscale morphology was beneficial for catalytic activity.

Introduction

Given the growing global demand for energy, one of the most important challenges of the century will likely involve developing

a cheap and active material for solar water splitting. Currently, however, no economically competitive water-splitting photocatalysts have been marketed mainly due to low overall conversion efficiencies and photocorrosion. Nano-scaling of bulk metal-oxide/sulfide/selenides offers new opportunities to develop more efficient catalysts, by taking advantage of increased surface area, shorter paths for charge and mass transport, and quantum confinement effects. Cadmium selenide, for example, can be activated for photocatalytic water reduction using a quantum size effect.^{1,2} Iron oxide (α -Fe₂O₃, hematite) is an attractive candidate for photocatalytic water oxidation, due to its low cost,

^aDepartment of Chemistry, University of California, Davis One Shields Avenue, Davis, CA, 95616, USA. E-mail: fosterloh@ucdavis.edu; Fax: (+1)530 752 8995

^bDepartment of Chemical Engineering and Materials Science, University of California, Davis One Shields Avenue, Davis, CA, 95616, USA

^cLawrence Livermore National Laboratory, 7000 East Avenue, Livermore, CA, 94550, USA

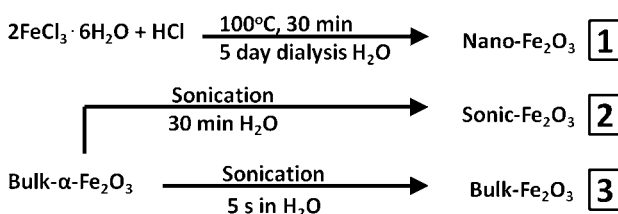
Broader context

Nanostructured alpha-Fe₂O₃ (hematite) has recently emerged as an inexpensive and stable photoanode material for photoelectrochemical water oxidation. Such photoanodes help facilitate direct sunlight driven water photoelectrolysis by which solar energy is converted into hydrogen fuel. The enhanced properties of nano-Fe₂O₃ are generally attributed to improved hole collection at the surface, enabled by the reduced dimensions of the nanocrystals. However, one can not rule out that part of the enhancement stems from impurity atoms such as silicon and tin which are introduced during the preparation of the photoanodes. Here we show for the first time, that photocatalytic water oxidation can be achieved also with suspended hematite particles, in the absence of any dopants. We find that the activity of the particles scales inversely with size, and that it is limited by deposition of silver onto the particles-a side effect of using silver nitrate as sacrificial electron acceptor. Even though the quantum efficiency remains below 1.0% for the smallest studied nanocrystals, the results highlight the validity of the nanoscaling approach for increasing photocatalytic activity in materials with short minority carrier lifetimes.

abundance, low toxicity, high photo/heat-stability, suitable band gap ($E_g = 2.06$ eV, $\lambda = 600$ nm) and valance band edge position. Despite these attributes, however, $\alpha\text{-Fe}_2\text{O}_3$ is considered to be a poor photo-anode material for water oxidation due to its short hole diffusion length (2–4 nm),³ short exciton lifetime (~ 10 ps),^{4,5} poor minority charge carrier mobility (0.2 cm 2 V $^{-1}$ s $^{-1}$),⁶ and finite light penetration depth ($\alpha^{-1} = 118$ nm at $\lambda = 550$ nm).⁷ Attempts to circumnavigate these issues involve a combination of surface modifications to reduce water oxidation overpotentials along with surface morphology control to increase current density.⁸ This includes selective growth of thin films on the most active crystal face (001) for more efficient electron and hole transport,⁹ and doping with metal cations including Mg $^{2+}$, Al $^{3+}$, Ca $^{2+}$, Ti $^{4+}$, V $^{5+}$, Cu $^{2+}$, Zn $^{2+}$, Nb $^{5+}$, Sn $^{4+}$, Pt $^{4+}$ and CO $_2^{+}$.^{11–16} Another approach to mitigate these problems is by nanostructuring Fe $_2\text{O}_3$. Kay *et al.* demonstrated that nanostructured Fe $_2\text{O}_3$ films grown by vapor deposition of Fe(CO) $_5$ /tetraethoxysilane could support photocurrent densities of up to 2.2 mAcm $^{-2}$ and incident photon to electron conversion efficiencies (IPCEs) of up to 42% at 1.23 eV *vs.* RHE.¹⁰ In another example, Fe $_2\text{O}_3$ photoelectrodes were fabricated from Fe $_2\text{O}_3$ nanocrystals, followed by an annealing step.¹⁷ These electrodes showed increased water oxidation activity, but also contained Si and Pt dopants that lead to increased conductivity. Similar Fe $_2\text{O}_3$ electrodes have been fabricated from Fe $_3\text{O}_4$ particles followed by annealing.¹⁸ To evaluate the effect of nanostructuring in the absence of doping, we report here on photocatalytic water oxidation with suspended bulk and nanoparticulate $\alpha\text{-Fe}_2\text{O}_3$. The study shows for the first time, that individually suspended Fe $_2\text{O}_3$ particles catalyze water oxidation with up to 0.61% quantum efficiency (at 375 nm) in the presence of a chemical bias (+0.70 V, NHE from 20.0 mM AgNO $_3$). The activity is inversely dependent on particle size, which we attribute to improved charge transport to the surface in the smaller particles. We also find that chemically synthesized particles have a significantly lower electrochemical overpotential for water oxidation than particles derived from bulk Fe $_2\text{O}_3$.

Results and discussion

Scheme 1 summarizes pathways to Nano-Fe $_2\text{O}_3$ [1], Sonic-Fe $_2\text{O}_3$ [2], and Bulk-Fe $_2\text{O}_3$ [3] as photocatalysts for this study. Suspensions of Bulk-Fe $_2\text{O}_3$ were produced by briefly (5 s) sonicating commercial alpha-Fe $_2\text{O}_3$ (hematite) in water. To obtain nanoscale materials, Fe $_2\text{O}_3$ was sonicated at a higher intensity for 30 min. As an alternative to this top-down approach, Nano-Fe $_2\text{O}_3$ was prepared from FeCl $_3$ in aqueous HCl using the published procedure by Raming *et al.*¹⁹



Scheme 1 Bottom-up approach to give Nano-Fe $_2\text{O}_3$ [1] and top-down approach to prepare Sonic-Fe $_2\text{O}_3$ [2] from Bulk-Fe $_2\text{O}_3$ [3]. Sonication was performed with an ultrasonic horn at 3.65 W.

Fig. 1 shows the powder XRD spectra of the three samples. For Bulk-Fe $_2\text{O}_3$ and Sonic-Fe $_2\text{O}_3$, all diffraction peaks can be assigned to the alpha phase of hematite. Due to lattice confinement, the Nano-Fe $_2\text{O}_3$ diffraction pattern consists of wider peaks and larger Full width at half maximum (FWHM) including an unexpected peak at 47° signifying the presence of $\beta\text{-FeOOH}$ (411 peak),²⁰ a known intermediate during aqueous synthesis of hematite.²¹ From the FWHM values of the (113) diffraction peak at 40°, Scherrer diameters were calculated as 120 nm for Bulk-Fe $_2\text{O}_3$, 44 nm for Sonic-Fe $_2\text{O}_3$, and 5.4 nm for Nano-Fe $_2\text{O}_3$. These values are in good agreement with data obtained from transmission electron microscopy in Fig. 2.

According to TEM/HRTEM, Bulk-Fe $_2\text{O}_3$ consists of large irregular and polydispersed (50–300 nm) crystals showing characteristic (001) lattice spacing of $\alpha\text{-Fe}_2\text{O}_3$ (Fig. 2a, b). Comparatively, Sonic-Fe $_2\text{O}_3$ shows smaller (5–20 nm) fragmented particles with irregular shapes, and lesser defined surfaces (Fig. 2e, f). In contrast, Nano-Fe $_2\text{O}_3$ images display a range of single crystalline spheres (5.2 ± 1.0 nm) interdispersed with rods (5.0 ± 0.8 nm \times 15.2 ± 1.1 nm, Fig. 2i, j).

Diffuse reflectance spectra for the three materials are shown in Fig. 3 and plotted with the Kubelka-Munk function. The band edge at 600 nm corresponds to a 2.06 eV band gap for each material. There is also a direct UV transition LMCT at 375 nm peak ($6t_{1u} \rightarrow 2t_{2g}$, 375 nm, not shown) and an indirect visible d-d transition ($^6A_1 \rightarrow ^4E$, 535 nm).²² This d-d transition is slightly blue shifted for Nano-Fe $_2\text{O}_3$ which accounts for the observed differences in color: Bulk-Fe $_2\text{O}_3$ (light red/orange), Sonic-Fe $_2\text{O}_3$ (pink/orange), and Nano-Fe $_2\text{O}_3$ (dark blood red, orange when diluted). The difference in slope between Nano-Fe $_2\text{O}_3$ and the other two is likely caused by the presence of small amounts of $\beta\text{-FeOOH}$ in the sample (a yellow precursor to $\alpha\text{-Fe}_2\text{O}_3$,²³ $E_g = 2.12$ – 2.35 eV).²⁰ The plot also shows a characteristic sub-band

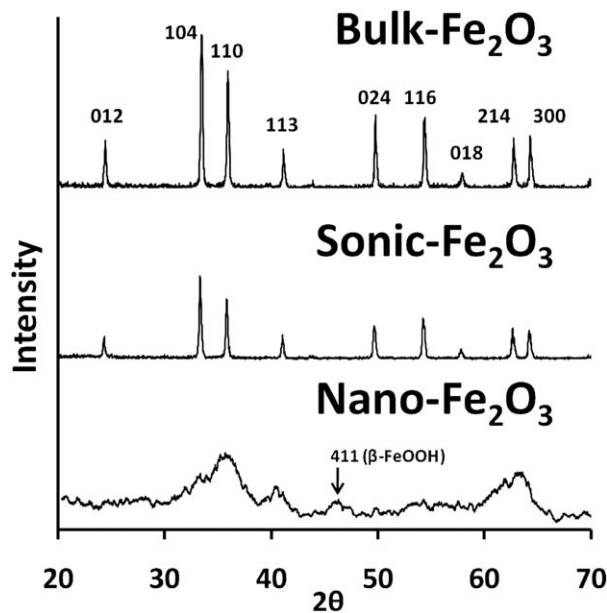


Fig. 1 Powder X-ray diffraction patterns of Bulk-Fe $_2\text{O}_3$, Sonic-Fe $_2\text{O}_3$, and Nano-Fe $_2\text{O}_3$. The patterns are in agreement with the alpha structure type, with Nano-Fe $_2\text{O}_3$ also containing traces of $\beta\text{-FeOOH}$.

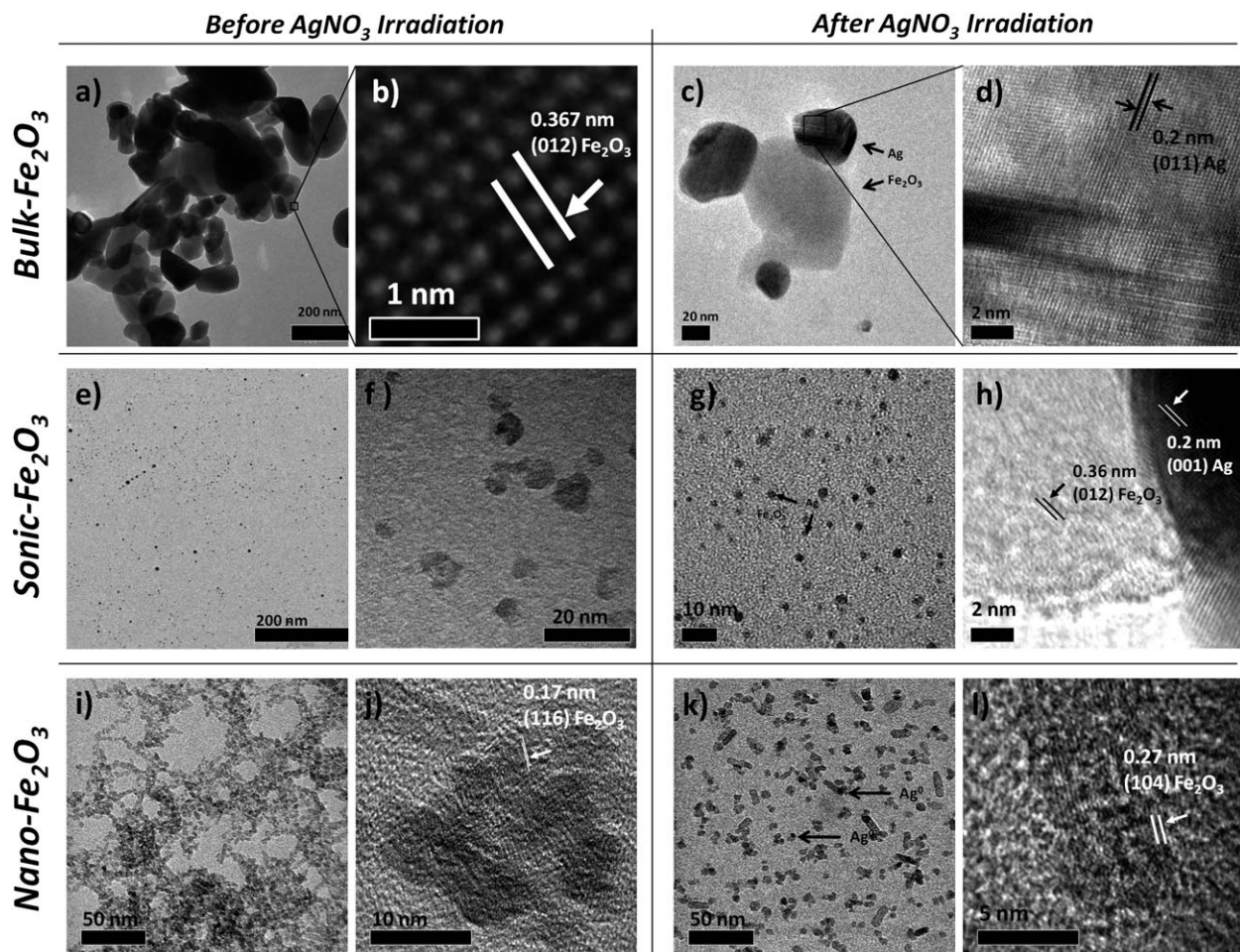


Fig. 2 TEM (a,e,f) and HRTEM of non-irradiated α - Fe_2O_3 (a,b,e,f,i,j) and after full-spectrum AgNO_3 irradiation (c,d,g,h,k,l). Bulk- Fe_2O_3 (a–d), Sonic- Fe_2O_3 (e–h), and Nano- Fe_2O_3 (i–l). Image g is not representative of particle size. It was chosen to demonstrate silver particle formation.

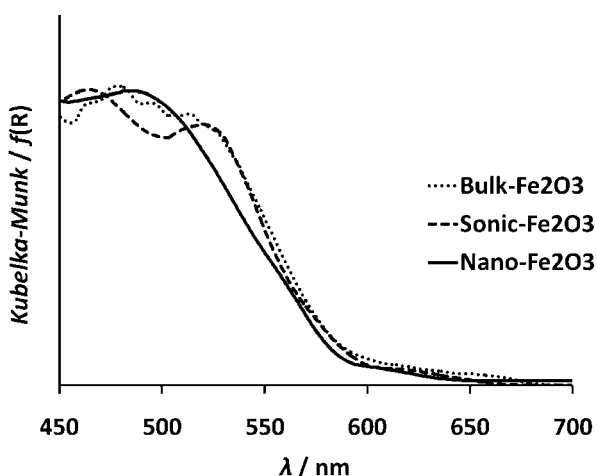


Fig. 3 Kubelka-Munk converted UV/Vis diffuse reflectance spectra of dried Bulk- Fe_2O_3 , Sonic- Fe_2O_3 and Nano- Fe_2O_3 catalysts.

scattering tail near 600–750 nm. The scattering intensity of this tail is known to increase with particle size.¹⁷

To test photocatalytic properties, the Fe_2O_3 powders were suspended in 20.0 mM aqueous AgNO_3 and irradiated with

a 300 W Xe-arc lamp equipped with a longpass filter (>400 nm) or without it (>250 nm). Under these conditions, oxygen is formed from photogenerated holes (Fig. 5) while silver is formed from photogenerated electrons. The deposition of silver can be

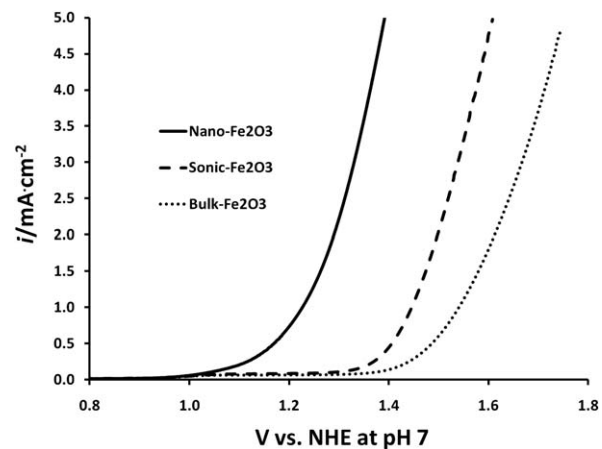


Fig. 5 Electrochemical water oxidation with Fe_2O_3 films on Au substrate, 50 mV/s scans, at pH = 7 in $\text{Na}_2\text{HPO}_4/\text{NaH}_2\text{PO}_4$ buffer.

observed in TEMs of the Fe_2O_3 particles. Images for post-irradiated Bulk- Fe_2O_3 (Fig. 2c and 2d) show the 0.2 nm characteristic lattice spacing of Ag (011). In Fig. 2g, Ag deposition is not as clear for Sonic- Fe_2O_3 due to the small size, except that the overall solution color became darker and greyer after irradiation. One Ag particle on Sonic- Fe_2O_3 is shown in Fig. 2h. Likewise, Nano- Fe_2O_3 shows evidence of silver deposition onto the nanocrystals. Here, we observe preferential deposition onto one facet, most likely the (001) facet, which can be explained by a higher anisotropic conductivity in this direction.⁹ Notably, the material retains its crystallinity after 24 h full spectrum irradiation (Fig. 2l) with no signs of photocorrosion (apart from Ag deposition).

Comparing photoactivity among samples and conditions, the highest O_2 evolution rates are obtained under full spectral irradiation (>250 nm, Fig. 4A). During the first 10 min, evolution rates range from $250 \mu\text{mol h}^{-1} \text{ g}^{-1}$ (for Bulk- Fe_2O_3) to $1071 \mu\text{mol h}^{-1} \text{ g}^{-1}$ (for Nano- Fe_2O_3). However, with the advent of silver deposition, O_2 evolution begins to decline. For Bulk- Fe_2O_3 this happens after 8 h, for Sonic- Fe_2O_3 after 10 h, and for Nano- Fe_2O_3 after 5 h. After 24 h, turnover numbers (TON = moles of O_2 evolved per mole of Fe_2O_3) reach values above unity (1.13 for Nano- Fe_2O_3 , 1.10 for Sonic- Fe_2O_3 and 0.49 for Bulk- Fe_2O_3), supporting a catalytic process for the nanomaterials. Apart from silver deposition, no change of the Fe_2O_3 is apparent (Fig. 2). This suggests that higher turnover numbers should be possible with other sacrificial agents. Under visible irradiation (>400 nm, Fig. 4B) the rates are notably lower, and as a consequence, TON numbers after 24 h (0.73 for Nano- Fe_2O_3 , 0.38 for Sonic- Fe_2O_3 and 0.08 for Bulk- Fe_2O_3) remain below unity. The lower activity under visible illumination is expected from both the lower absorbance of the material and from the less oxidizing power of holes created in the Fe-t_{2g} band (see discussion of Fig. 6).

The initial O_2 evolution rates of the three systems are plotted in Fig. 4C as a function of size. It can be seen that for both visible and UV irradiation, the rate increase is inversely proportional to the logarithm of particle diameter. For visible light ($\lambda > 400$ nm), the slope is lower, because of the reliance of the photoreaction on the weaker d-d transition (see discussion of Fig. 6). Also, visible light penetrates deeper into the particles than UV light, reducing illumination-based differences among particles of different size. Improved illumination under visible light might be responsible for the high initial activity (first two hours) of Sonic- Fe_2O_3 that rivals that of Nano- Fe_2O_3 (Fig. 4B). However, as particle shading increases with silver deposition, the activity of the larger Sonic- Fe_2O_3 particles falls behind that of the smaller Nano- Fe_2O_3 . Although shading effects do seem to play a role in these systems, the observed size trend in the activity of the Fe_2O_3 samples can be understood well in terms of the short hole diffusion length (2–4 nm)³ of hematite. Only holes generated within a 3 nm thick subsurface shell can participate in water oxidation. By comparing the volume of this shell in each sample with the total volume of the particles (assuming spheres), one can calculate the fraction of usable e/h pairs as a function of size (diameters taken from powder X-ray diffraction). The values are 14.3% for Bulk- Fe_2O_3 , 35.6% for Sonic- Fe_2O_3 , and 100% for Nano- Fe_2O_3 —since it is less than 6 nm wide. This increased hole availability at the surface of the smaller particles can fully explain the observed trend in oxygen evolution across the series (Fig. 4). However, as additional irradiations with monochromatic light from a LED (375 nm) show,

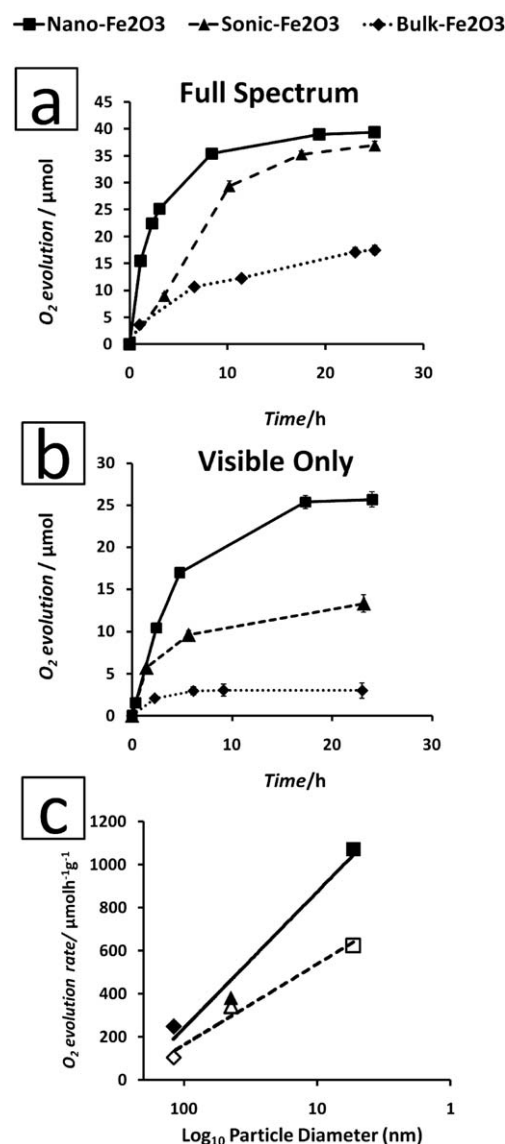


Fig. 4 O_2 evolution from $35 \mu\text{mol}$ (5.6 mg) $\alpha\text{-Fe}_2\text{O}_3$ in 20.0 mM AgNO_3 at $\text{pH} = 6.5$ under full spectrum irradiation (a) and under visible light, $\lambda > 400$ nm (b). Error Bars represent deviations of two separate experiments. (C) Relation between initial rate of water oxidation ($\mu\text{mol O}_2 \text{ h}^{-1} \text{ g}^{-1}$) and average Scherrer crystallite diameter (nm) derived from Fig. 1 in full spectrum irradiation (solid line) and in visible light (broken line) for Bulk- Fe_2O_3 (diamond), Sonic- Fe_2O_3 (triangle) and Nano- Fe_2O_3 (square).

the fraction of holes that *actually* oxidize water is much lower than the number of holes created within 3 nm of the surface. Based on the observed O_2 generation rates under LED illumination ($1.13 \times 10^7 \text{ mol s}^{-1}$ at the flask surface), we calculate quantum efficiencies (QE) of 0.61%, 0.47%, and 0.0% for Nano-, Sonic-, and Bulk- Fe_2O_3 , respectively. Here we assume that four photons/holes are required to form one molecule of O_2 . The numbers show that even in Nano- Fe_2O_3 , >97% of the generated charge carriers recombine before they react with water. This demonstrates that the reactivity of the nanocrystals is still limited by charge recombination (the half life of e/h pairs in hematite is ~ 10 ps).^{4,5} The problem of enhanced surface recombination in Fe_2O_3 is well known.²⁴ Surface recombination can be reduced by terminating

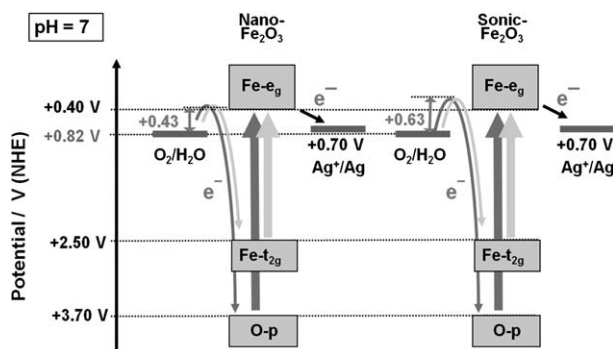


Fig. 6 Energy diagram for photocatalytic water oxidation at pH = 7 with 20.0 mM AgNO₃ as a sacrificial acceptor. The ‘dark’ water oxidation overpotentials at 1.0 mA are included as an approximation for the charge transfer limitation at the Fe₂O₃-electrolyte interface. This is not technically correct, as the dark anodic current is mediated by conduction band states in Fe₂O₃, whereas the light current involves states in the Fe₂O₃ valence band.^{29,30}

the surface with closed shell ions (Al³⁺, Sn⁴⁺, Si⁴⁺), as several research groups have shown recently.^{12,16,25}

In order to further probe the differences in reactivity between the Fe₂O₃ samples, electrochemical measurements were conducted on thin films of the materials. The voltammetric scans in Fig. 5 show that the electrochemical onset potentials for water oxidation are different for each particle size, with onsets occurring between +1.25 and +1.40 V (NHE, 1.0 mA cm⁻²). Based on the thermodynamic minimum water oxidation potential of +0.82 V vs. NHE at pH 7, the overpotentials (measured at 1.0 mA cm⁻²) are $\eta = +0.43$ V (Nano-Fe₂O₃), $\eta = +0.63$ V (Sonic-Fe₂O₃), and $\eta = +0.72$ V (Bulk-Fe₂O₃), respectively. This data is comparable to values published in the literature for alpha-Fe₂O₃ films (+0.57 V^{10,15} and +0.47 V¹⁶) after adjustment to pH = 7. This difference in potentials between Sonic- and Nano-Fe₂O₃ is likely due to differences in surface structure. As a product of cavitation-induced particle fragmentation,²⁶ Sonic-Fe₂O₃ particles have a rough surface dominated by high index planes. This can be seen well in Fig. 2h. Nano-Fe₂O₃ on the other hand, is a product of strain-free growth, which favors the formation of stable low index facets. The effect of the surface structure on the reactivity of hematite nanocrystals was observed previously by Hermanek *et al.*²⁷

Fig. 6 shows potential diagrams for Nano- and Bulk-Fe₂O₃, based on the literature value of E_{CB} = +0.40 V for the conduction band edge of alpha-Fe₂O₃ at pH = 7,²⁸ and based on the optical band gaps for the d-d and LMCT transitions. Holes for oxygen evolution can be generated either in Fe-t_{2g} orbitals (visible light excitation) or in the O-p band (UV excitation). Holes in the O-p band are more oxidizing, which is one reason for the greater O₂ evolution activity of Fe₂O₃ under UV excitation (besides increased light absorption in the UV). As the diagram shows, most of the energy of the holes is consumed during water oxidation. Based on the electrochemical results, Nano-Fe₂O₃ has a slightly lower energetic barrier for injecting holes into water than Sonic- and Bulk-Fe₂O₃ (the water oxidation overpotential is +0.43 V compared to +0.63 V for Sonic-Fe₂O₃, see caption in Fig. 6). This is an additional reason for the higher activity of Nano-Fe₂O₃, besides more efficient hole collection at the surface, as discussed above.

The diagram further shows that the oxygen evolution requires an electrochemical bias (about +0.70 V for 20.0 mM AgNO₃ at pH = 7), higher than what has been described for nanostructured α -Fe₂O₃ photoanodes (+0.39 V, NHE at pH 7).¹⁰ Thus, the thermodynamic driving force for electron transfer from the Fe₂O₃ conduction band edge to the silver ion acceptor is 0.30 eV per electron. Because the silver reduction potential of 0.70 V is less than the water oxidation potential (0.82 V at pH = 7), conversion of a fraction of the light energy into chemical energy is observed (0.12 eV per converted photon). However, because the quantum yield is so small (less than 1%), the overall process remains strongly exergonic.

Conclusion

In conclusion, we have shown that suspended crystals of non-doped alpha-Fe₂O₃ are active for photocatalytic O₂ evolution under visible and UV light with initial rates of up to 1072 $\mu\text{mol h}^{-1}\text{g}^{-1}$ for Nano-Fe₂O₃. Under visible light the activity is 767 $\mu\text{mol h}^{-1}\text{g}^{-1}$. Even though silver surface deposition limits the water oxidation ability of the materials, turnover numbers above unity were achieved for nanocrystals of Fe₂O₃, but not for the bulk. Activity is correlated inversely with the size of the crystals, *i.e.* Nano-Fe₂O₃ is more active than Bulk-Fe₂O₃, which can be explained with a reduced hole diffusion path to the surface. However as the low quantum efficiencies of 0.61% show, activities in all three systems are limited strongly by surface charge recombination. Also, we find that Nano-Fe₂O₃ crystals have a low water oxidation overpotential of 0.43 V (at 1.0 mA cm⁻²), which we attribute to a favorable surface structure of the material. This is the first time that direct catalytic O₂ generation from Fe₂O₃ was achieved *via* UV and visible light irradiation in homogeneous phase. The results show that nanoscaling increases the photoactivity of Fe₂O₃. Similar nanoscaling strategies may be applicable to other transition metal oxides.

Experimental

Chemicals (α -Fe₂O₃ 99.9%, AgNO₃ 99.9%, FeCl₃·6H₂O 99.9%, and 12.1 N HCl 99.99%) were purchased from Fisher Scientific, Pittsburgh, PA. They were of reagent quality and were used as received. Water was purified to 18 MΩcm resistivity using a Nano-pure system. Bulk-Fe₂O₃ was prepared with as-purchased α -Fe₂O₃ and dissolved in water followed by a 5 s sonication with a Fisher Scientific FS20 ultrasonic cleaner to disperse the colloid. Sonic-Fe₂O₃ was prepared by ultrasonication of Bulk-Fe₂O₃ for 30 min with a Sonics Vibracel™ VCX130 ultrasonic horn at 20% power (3.65 W) in 30 mL of H₂O. Nano-Fe₂O₃ was synthesized following a literature method¹⁹ by dissolving FeCl₃·6H₂O into 250 mL of 0.002 M HCl at 100 °C to make a 0.02 M Fe³⁺ solution with stirring. After maintaining the temperature for 30 min, the heat was removed and the solution was allowed to return to room temperature. Excess spectator ions (Fe³⁺, H⁺ and Cl⁻, etc.) were removed during a 5 day dialysis using 6–8 k MWCO tubing in 4 L water. The water was replaced daily until the conductivity reached 4.0 $\mu\text{S cm}^{-1}$. Full chloride removal is important during this step to avoid formation of photoactive AgCl during irradiation.³¹ The

final suspension contained 1.12 mg mL^{-1} of Fe_2O_3 as determined by gravimetric analysis.

Transmission electron images were taken with a Philips CM-12 instrument at 120 kV acceleration potential. Bright field high resolution transmission electron microscopy (HRTEM) images were taken using a JEOL 2500SE 200kV TEM. Copper grids with a carbon film were dropped into aqueous dispersions of the samples followed by washing with water and air drying.

UV/Vis diffuse reflectance spectra were taken as dried powders on white Teflon tape using an Ocean Optics HR2000 CG-UVNIR spectrometer and a DH2000 light source. Reflectance was converted to Kubelka-Munk as $f(R) = (1 - R)^2(2R)^{-1}$ vs. wavelength to correct for scattering.

For electrochemical measurements thin films of the catalysts were prepared on a gold foil electrode (1.0 cm^2) by dropcoating and annealing at 450°C . The films were then pressed with a CARVER 4350.L steel press to 15000 psi following literature procedures.³² A wire was attached to the bare gold back with conductive carbon tape and sealed with adhesive. The electrode was placed into a N_2 -purged 3-electrode cell with a Pt counter electrode and a saturated calomel reference electrode connected to the cell with a KCl salt bridge. The cell was filled to 50 mL with 0.25 M $\text{Na}_2\text{HPO}_4/\text{NaH}_2\text{PO}_4$ buffer solution at pH 7 with a constant stream of N_2 above the solution. Dark cyclic voltammetry scans were taken at 50 mV/s. The system was calibrated using the redox potential of $\text{K}_4[\text{Fe}(\text{CN})_6]$ at $+0.358 \text{ V}$ (NHE).

The rate of photochemical oxygen evolution from each catalyst was determined by irradiating 5.6 mg (35 μmol) of Fe_2O_3 in 20.0 mM AgNO_3 in 50 mL of water. Silver nitrate was chosen as a sacrificial agent because it is stable under UV irradiation and does not cause aggregation of the nanoparticles (as observed with ferric nitrate, cerium (IV) ammonium nitrate, sodium iodate, and sodium persulfate). Irradiations were performed in a quartz round bottom flask with a 300 W Xe arc lamp (1.4 W cm^{-2} at flask, $\lambda = 250\text{--}680 \text{ nm}$), measured with a UV/Vis GaAsP photodetector. Visible light ($\lambda > 400 \text{ nm}$) was achieved by inserting a 400 nm long-pass filter between the light and the flask. The air-tight irradiation system connects a vacuum pump and a gas chromatograph (Varian 3800) with the sample flask to quantify the amount of gas evolved, using area counts of the peaks and the identity of the gas from the calibrated carrier times. Prior to irradiation, the flask was evacuated down to 5 torr and purged with argon gas. This cycle was repeated until the chromatogram of the atmosphere above the solution indicated that the sample did not contain hydrogen, oxygen, or nitrogen. A solution of 20.0 mM AgNO_3 was tested as a control under full spectrum irradiation, and less than 3 μmol of O_2 were evolved after 10 h. Quantum efficiency measurements were conducted with a 375 nm LED (3.42 mW cm^{-2} , $1.13 \times 10^{17} \text{ photon s}^{-1}$) in place of the lamps.

Powder XRD scans were conducted with a Scintag XRD, $\lambda = 0.154 \text{ nm}$ at -45 kV and 40 mA with tube slit divergence(2 mm), scatter(4 mm), column scatter(0.5 mm), and receiving(0.2 mm). The FWHM of the peaks were calculated with ThemoARL DMSNT software (version 1.39-1).

Acknowledgements

FEO thanks Research Corporation for Science Advancement for a Scialog award. This work was further supported by the

National Science Foundation (NSF, grant 0829142) and by the US Department of Energy under grant number FG02-03ER46057. TKT thanks NSF for a Graduate Research Fellowship 2011.

Notes and references

- 1 F. A. Frame, E. C. Carroll, D. S. Larsen, M. Sarahan, N. D. Browning and F. E. Osterloh, *Chem. Commun.*, 2008, 2206–2208.
- 2 F. A. Frame and F. E. Osterloh, *J. Phys. Chem. C*, 2010, **114**, 10628–10633.
- 3 (a) J. H. Kennedy and K. W. Frese, *J. Electrochem. Soc.*, 1977, **124**, C130–C130; (b) K. L. Hardee and A. J. Bard, *J. Electrochem. Soc.*, 1976, **123**, 1024–1026.
- 4 A. G. Joly, J. R. Williams, S. A. Chambers, G. Xiong, W. P. Hess and D. M. Laman, *J. Appl. Phys.*, 2006, **99**, 6.
- 5 N. J. Cherepy, D. B. Liston, J. A. Lovejoy, H. M. Deng and J. Z. Zhang, *J. Phys. Chem. B*, 1998, **102**, 770–776.
- 6 A. J. Bosman and H. J. Vandaal, *Adv. Phys.*, 1970, **19**, 1–7.
- 7 K. Itoh and J. O. Bockris, *J. Electrochem. Soc.*, 1984, **131**, 1266–1271.
- 8 K. Sivula, F. L. Formal and M. Gratzel, *ChemSusChem*, 2011, **4**, 432–449.
- 9 C. M. Eggleston, A. J. A. Shankle, A. J. Moyer, I. Cesar and M. Gratzel, *Aquat. Sci.*, 2009, **71**, 151–159.
- 10 A. Kay, I. Cesar and M. Gratzel, *J. Am. Chem. Soc.*, 2006, **128**, 15714–15721.
- 11 S. Mohanty and J. Ghose, *J. Phys. Chem. Solids*, 1992, **53**, 81–91.
- 12 J. A. Glasscock, P. R. F. Barnes, I. C. Plumb and N. Savvides, *J. Phys. Chem. C*, 2007, **111**, 16477–16488.
- 13 T. Arai, Y. Konishi, Y. Iwasaki, H. Sugihara and K. Sayama, *J. Comb. Chem.*, 2007, **9**, 574–581.
- 14 C. J. Sartoretti, B. D. Alexander, R.olarska, W. A. Rutkowska, J. Augustynski and R. Cerny, *J. Phys. Chem. B*, 2005, **109**, 13685–13692.
- 15 Y. S. Hu, A. Kleiman-Shwarzstein, A. J. Forman, D. Hazen, J. N. Park and E. W. McFarland, *Chem. Mater.*, 2008, **20**, 3803–3805.
- 16 R. L. Spray, K. J. McDonald and K. S. Choi, *J. Phys. Chem. C*, 2011, **115**, 3497–3506.
- 17 K. Sivula, R. Zboril, F. Le Formal, R. Robert, A. Weidenkaff, J. Tucek, J. Frydrych and M. Gratzel, *J. Am. Chem. Soc.*, 2010, **132**, 7436–7444.
- 18 R. H. Goncalves, B. H. R. Lima and E. R. Leite, *J. Am. Chem. Soc.*, 2011, **133**, 6012–6019.
- 19 T. P. Raming, A. J. A. Winnubst, C. M. van Kats and A. P. Philipse, *J. Colloid Interface Sci.*, 2002, **249**, 346–350.
- 20 Y. Xiong, Y. Xie, S. W. Chen and Z. Q. Li, *Chem.–Eur. J.*, 2003, **9**, 4991–4996.
- 21 R. S. Sapienza, R. C. Patel and E. Matijevic, *J. Phys. Chem.*, 1977, **81**, 1061–1068.
- 22 L. A. Marusak, R. Messier and W. B. White, *J. Phys. Chem. Solids*, 1980, **41**, 981–984.
- 23 E. Matijevic and P. Scheiner, *J. Colloid Interface Sci.*, 1978, **63**, 509–524.
- 24 M. P. Dareedwards, J. B. Goodenough, A. Hamnett and P. R. Trevellick, *J. Chem. Soc., Faraday Trans. 1*, 1983, **79**, 2027–2041.
- 25 F. Le Formal, N. Tetreault, M. Cornuz, T. Moehl, M. Gratzel and K. Sivula, *Chem. Sci.*, 2011, **2**, 737–743.
- 26 K. S. Suslick and G. J. Price, *Annu. Rev. Mater. Sci.*, 1999, **29**, 295–326.
- 27 M. Hermanek, R. Zboril, I. Medrik, J. Pechousek and C. Gregor, *J. Am. Chem. Soc.*, 2007, **129**, 10929–10936.
- 28 Y. Xu and M. A. A. Schoonen, *Am. Mineral.*, 2000, **85**, 543–556.
- 29 H. Gerischer, Semiconductor electrode reactions In *Adv. Electrochem. & Electrochem. Eng.*, P. Delahay, Ed. Interscience: New York, 1961, **1**, 139–232.
- 30 A. J. Nozik and R. Memming, *J. Phys. Chem.*, 1996, **100**, 13061–13078.
- 31 M. Lanz, D. Schurch and G. Calzaferri, *J. Photochem. Photobiol. A*, 1999, **120**, 105–117.
- 32 D. A. Totir, B. D. Cahan and D. A. Scherson, *Electrochim. Acta*, 1999, **45**, 161–166.